



Flexible electrospun iron/manganese-based compounds/carbon fibers: Phase transformation and electrochemical properties

Fei Xie^{a,1}, Xiaoli Sheng^{a,1}, Zhibin Ling^a, Shujin Hao^a, Qingye Zhang^a, Meng Sun^a,
Guanting Liu^{a,b}, Feiyu Diao^{b,*}, Yiqian Wang^{a,*}

^a College of Physics, Qingdao University, No. 308 Ningxia Road, Qingdao 266071, People's Republic of China

^b Industrial Research Institute of Nonwovens and Technical Textiles, Shandong Center for Engineered Nonwovens, College of Textiles and Clothing, Qingdao University, No. 308 Ningxia Road, Qingdao 266017, People's Republic of China

ARTICLE INFO

Keywords:

Carbon fibers
Electrospinning
Phase transformation
Anode materials
Electrochemical performance

ABSTRACT

Iron compounds have been extensively used as anode materials of lithium-ion batteries because of their low-cost and excellent electrochemical performance. However, iron compounds have a poor cyclic stability as a result of their drastic volume change in the charge/discharge processes. Herein, we propose an effective strategy to improve the cyclic performance of iron compounds by carbon coating and mixing with manganese oxide. To implement this, flexible carbon fibers embedded with Fe/Mn-based nanoparticles are produced by electrospinning with subsequent annealing process. By adjusting the annealing temperatures, the phase transformation of Fe/Mn-based compounds within carbon fibers is investigated in details. As the annealing temperature increases, Fe/Mn precursors (iron acetylacetonate and manganese acetylacetonate) in the fibers decompose gradually and then Fe₃O₄ and MnO nanoparticles form successively. When the temperature rises to 800 °C, the formed Fe₃O₄ is gradually reduced by carbon to produce Fe₃C while MnO remains unchanged. The carbon fibers loaded with different Fe/Mn-based compounds (Fe₃O₄, Fe₃O₄/MnO, Fe₃O₄/Fe₃C/MnO and Fe₃C/MnO) are obtained under different annealing temperatures. Among these composites, carbon fibers loaded with Fe₃O₄/Fe₃C/MnO nanoparticles exhibit the best specific capacity (750.23 mAh g⁻¹ after 250 cycles) and cyclic stability, ascribing to the synergistic effect of iron and manganese compounds. Furthermore, it is found that charge transfer impedance of the anodes is reduced and Li⁺ diffusion ability is improved as the annealing temperature increases, which is ascribed to the increasing content of Fe₃C and the short Li⁺ diffusion distance resulted from the reduced diameter of carbon fibers. The excellent electrochemical performance indicates that the hybrid electrospun nanofibers have a great potential application for flexible lithium-ion batteries.

1. Introduction

Transition metal compounds have become an important candidate as anode materials owing to their distinct advantages such as environmental friendliness, low cost and excellent electrochemical performance [1–4]. Among them, iron compounds, *i.e.* iron oxides [5,6] and iron carbide [7], have attracted extensive research attention due to their remarkable theoretical specific capacity and outstanding catalytic activity. Yet virtually iron compounds are heavily influenced by drastic volume change during charge/discharge cycling, which results in severe pulverization, leading to inferior cyclic stability [8]. Hence, it is urgent to find suitable strategies to enhance their cyclic stability.

To overcome iron compounds' volume expansion during the charge/discharge processes in lithium ion battery, diverse carbon materials such as graphene, carbon nanotubes and activated carbon have been extensively applied as a volume buffer to increase cycle stability of iron compounds [9–11]. For example, a composite composed of yolk-shell structured Fe₃O₄@C and Fe₃C, synthesized by Huang et al. [12], possessed a specific capacity of 600 mAh g⁻¹ after 300 cycles at a current density of 1000 mA g⁻¹ under ambient temperature, which was ascribed to the protective carbon shell and catalytic Fe₃C. Graphene/ α -Fe₂O₃ nanostructures prepared by Zhang et al. [13], kept a reversible specific capacity of 607 mAh g⁻¹ after 100 cycles at a current density of 100 mA g⁻¹ due to the introduction of graphene which can alleviate the volume

* Corresponding authors.

E-mail addresses: fydiao@qdu.edu.cn (F. Diao), yqwang@qdu.edu.cn (Y. Wang).

¹ These authors contributed equally to this work.

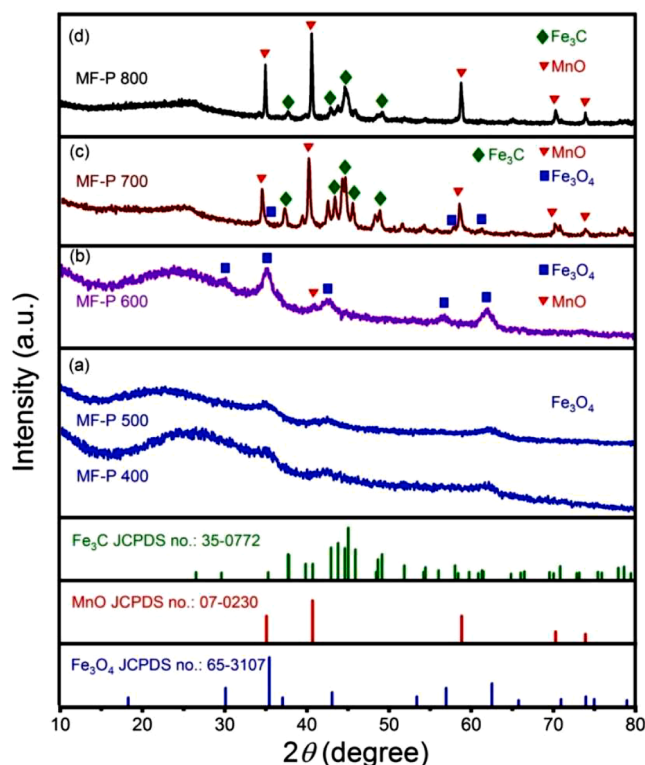


Fig. 1. XRD patterns of (a) MF-P 400 and MF-P 500, (b) MF-P 600, (c) MF-P 700 and (d) MF-P 800.

change of electrode materials during discharge/charge processes. Furthermore, compared to single metal oxide, mixed transition metal oxides usually exhibited better electrochemical performance [14–16]. Compared with iron compounds, manganese oxides [17] showed better cycling stability. Therefore, it is effective to optimize the cyclic stability of iron compounds by mixing with manganese oxides. In summary, the cycle stability of iron compounds can be enhanced more effectively by carbon coating and mixing with manganese oxides.

Great progress has been made on the improvement of electrochemical properties for iron compounds and their composites, but scarce reports can be found on their structural or phase evolution. For the iron compounds, Wang et al. [18] explored their phase evolution process in carbon fibers (CF) under different annealing temperatures. However, for the heterostructured metallic compounds in the CF, *i.e.*, Fe/Mn-based compounds, their phase evolution remains unclear. Thus, it is imperative to clarify the phase evolution of Fe/Mn-based compounds in the CF under different annealing temperatures, which can further help to improve their electrochemical performance.

In this work, heterogeneous flexible anode materials with Fe/Mn-based nanoparticles embedded in carbon fibers are prepared by electrospinning and subsequent annealing processes. Several Fe/Mn-based compounds, including Fe_3O_4 , $\text{Fe}_3\text{O}_4/\text{MnO}$, $\text{Fe}_3\text{O}_4/\text{Fe}_3\text{C}/\text{MnO}$ and $\text{Fe}_3\text{C}/\text{MnO}$, are produced in the carbon fibers as the annealing temperature increases. The phase transformation processes are investigated in details. Beside, through carbon coating and mixing with MnO, the volume expansion of iron compounds is alleviated during the electrochemical cycle process and their cycle stability is improved.

2. Experimental section

2.1. Materials

Polyacrylonitrile (PAN, average Mw. 150,000), Iron acetylacetonate [$\text{Fe}(\text{acac})_3$, 98 %], Manganese acetylacetonate [$\text{Mn}(\text{acac})_3$, 98 %], and

N, N-Dimethylformamide (DMF, 99.5 %) were purchased from Sino-pharm Chemical Reagent Co., Ltd. All chemicals were of analytical grade and used as received without further purification.

2.2. Preparation of Fe/Mn-based fiber membranes

First, the precursor solution containing DMF, PAN (11 wt.%), $\text{Fe}(\text{acac})_3$ and $\text{Mn}(\text{acac})_3$ (a molar ratio of 2:1) were prepared, and stirred at 30 °C for 6 h to form a viscous mixture. Then, the fiber membranes were obtained by electrospinning under a working voltage of 20 kV with a flow rate of 0.36 mL/h. The distance between needle tip and collecting roll was set as 16 cm. The speed of the receiver and the diameter of the needle were 500–800 rpm and 0.55 mm. The temperature and the humidity were 26 °C and 33–36 %. Subsequently, the as-prepared fiber membranes were stabilized in drying oven at 230 °C for 2 h. Finally, the stabilized fiber membranes were annealed with the temperature ranging from 400 to 800 °C for 2 h with a heating rate of 2 °C/min in argon atmosphere. The fiber films obtained at different annealing temperatures were labeled as MF-P T (T stands for annealing temperature). For example, the fiber membrane annealed at 400 °C was labeled as MF-P 400. For comparison, we prepared Fe or Mn-based fiber membranes by preparing precursor solution containing DMF, PAN (11 wt.%), $\text{Fe}(\text{acac})_3$ or $\text{Mn}(\text{acac})_3$, and then following the above electrospinning and annealing procedure. The fiber membranes obtained at 700 and 800 °C were marked as F-P 700, F-P 800, M-P 700 and M-P 800, respectively.

2.3. Materials characterization

The crystal structures of as-prepared fiber membranes were investigated using an X-ray diffractometer (XRD, Bruker D8 Advance) with $\text{Cu-K}\alpha$ radiation ($\lambda = 1.5406 \text{ \AA}$). Their morphologies were studied using a field-emission scanning electron microscope (FE-SEM, Sigma 500) at an accelerating voltage of 20 kV. Their compositions were determined using an energy dispersive X-ray spectrometer (EDS, Oxford INCA-

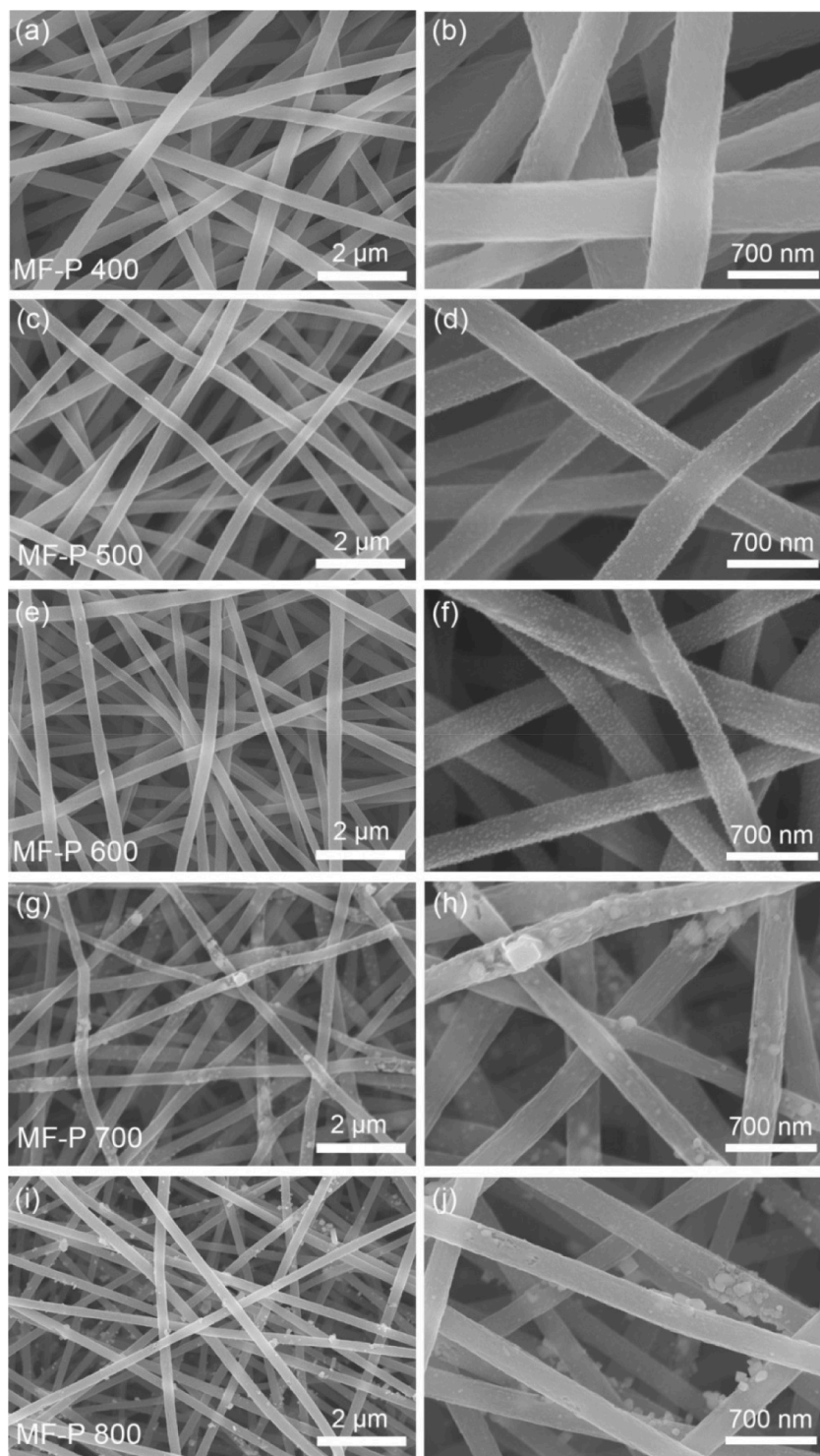


Fig. 2. FE-SEM images of MF-P 400 (a and b), MF-P 500 (c and d), MF-P 600 (e and f), MF-P 700 (g and h) and MF-P 800 (i and j).

Sight6427). The elemental mapping of MF-P 700 and 800 were carried out on EDS (Oxford INCAx-Sight6427). Bright-field (BF) and high-resolution transmission electron microscopy (HRTEM) images were obtained using a transmission electron microscope (TEM, JEOL JEM 2100F) at 200 kV. X-ray photoelectron spectra (XPS, Thermo Scientific K-Alpha+) were acquired with an Al K_{α} X-ray source ($h\nu = 1486.6$ eV). Thermogravimetric analysis (TGA, Germany NETZSCH TG209F3) was carried out at temperatures ranging from 30 to 900 °C with a heating rate of 10 °C/min.

2.4. Electrochemical measurements

The annealed fibers membranes (thickness about 200 μm , mass of composite about 2.0 mg) were used as the anode electrode material for LIBs and their lithium storage capacity were investigated. The assembly process for CR2025-type coin cells is carried out in a glove box filled with high-purity argon under the condition that both moisture and oxygen concentrations are less than 0.1 ppm. A mixture of 1 M LiPF_6 solution and ethylene carbonate (EC)/dimethyl carbonate (DMC)/diethyl carbonate (DEC) (1:1:1 vol ratio) was used as electrolyte and lithium foil

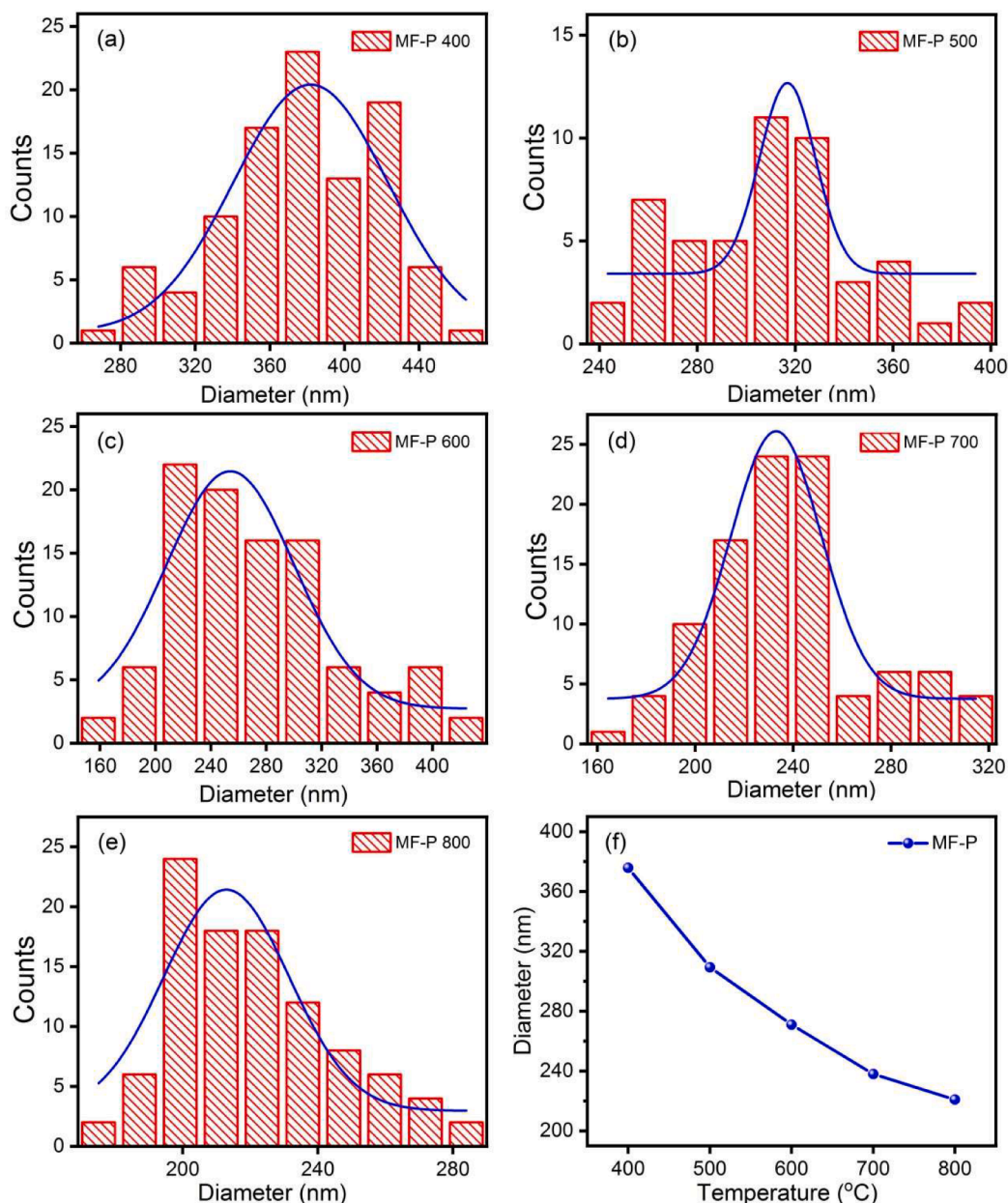


Fig. 3. Diameter distributions of (a) MF-P 400, (b) MF-P 500, (c) MF-P 600, (d) MF-P 700 and (e) MF-P 800. (f) Average diameters as a function of temperature for MF-P fibers.

was used as counter electrode. The rate performance and cycling stability were tested using a LAND CT2001 battery test system with a voltage range of 0.01–3.00 V. The cyclic voltammetry (CV) and electrochemical impedance spectroscopy (EIS) tests were carried out on a Metrohm Autolab electrochemical workstation (PGSTAT 302 N). At a scan rate of 0.3 mV s^{-1} , the CV curves with the potential range of 0.01–3.00 V were acquired. At the disturbance amplitude of 5 mV, the EIS spectra were gained with the frequency range of 100 kHz–0.01 Hz.

3. Results and discussion

To explore the crystal structure of different phases produced in the CF under different annealing temperatures, systematic XRD analysis was carried out. Fig. 1 shows the XRD patterns of the MF-P samples. As displayed in Fig. 1a, diffraction peaks of MF-P 500 and MF-P 400 have similar peak positions. The diffusive broad peak at 26° corresponds to amorphous carbon. The three peaks appeared at 35.4° , 43.1° and 62.5°

belong to the (311), (400) and (440) crystal planes of Fe_3O_4 (JCPDS no.: 65–3107, $a = 8.396 \text{ \AA}$) [19], suggesting that Fe_3O_4 nanocrystals are produced as annealing temperature rises to 400°C . The diffraction peaks of cubic phase MnO (JCPDS no.: 07–0230, $a = 4.445 \text{ \AA}$) [20] emerge in the XRD pattern of MF-P 600, as shown in Fig. 1b. The peak at 35.0° is caused by the overlapped diffraction of the (311) plane of Fe_3O_4 and the (111) plane of MnO [20], while the diffraction peak observed at 40.5° belongs to the (200) crystal plane of MnO, indicating that MnO is formed at 600°C . The mass ratio of Fe_3O_4 and MnO in MF-P 600 is determined to be 8:3 from quantitative analysis of its XRD pattern. Compared with MF-P 600, the XRD pattern of MF-P 700 shows the new diffraction peaks at 37.6° , 42.9° , 43.7° , 44.6° , 45.0° , 45.9° , 48.6° and 49.1° , corresponding to (121), (211), (102), (220), (031), (112), (131) and (221) crystal plane of the orthorhombic Fe_3C (JCPDS no.: 35–0772, $a = 5.0910 \text{ \AA}$, $b = 6.7434 \text{ \AA}$, $c = 4.5260 \text{ \AA}$, $\alpha = \beta = \gamma = 90^\circ$) [21], respectively. Thus, Fe_3O_4 , Fe_3C and MnO co-exist in MF-P 700. The mass ratio of Fe_3O_4 , MnO and Fe_3C in MF-P 700 is determined to be 0.5:1:3 from

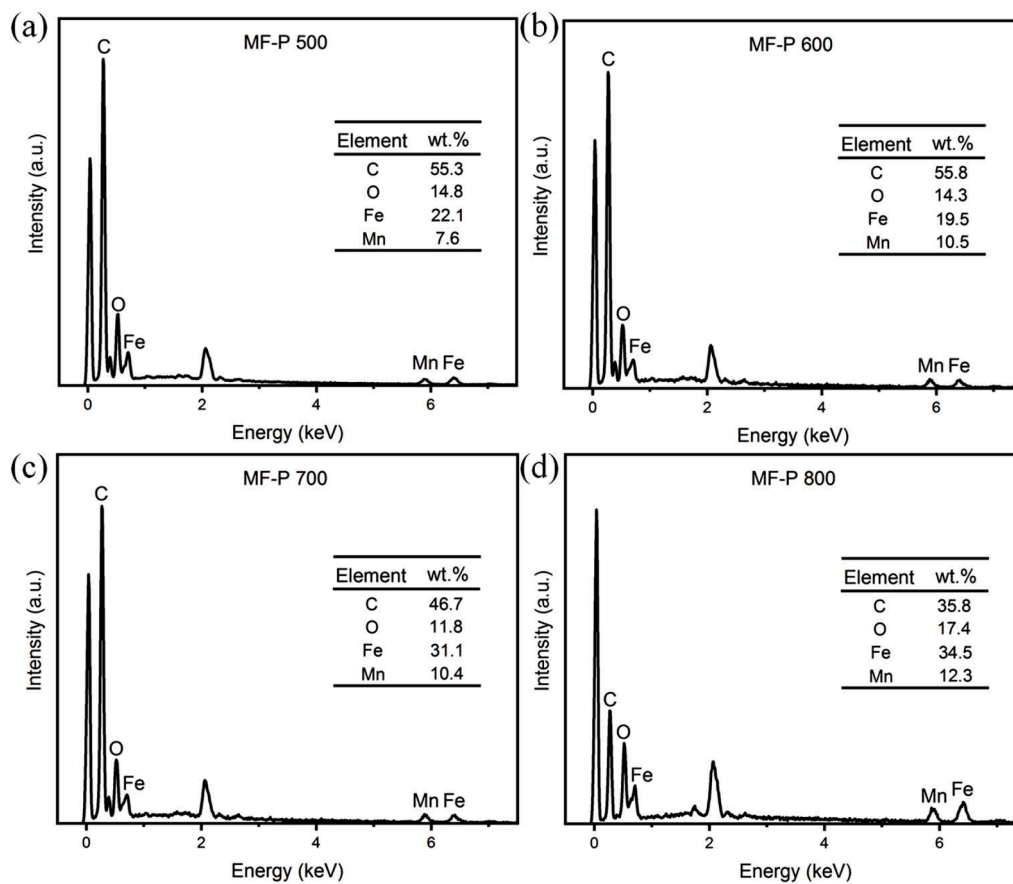


Fig. 4. EDS spectra acquired from (a) MF-P 500, (b) MF-P 600, (c) MF-P 700, (d) MF-P 800.

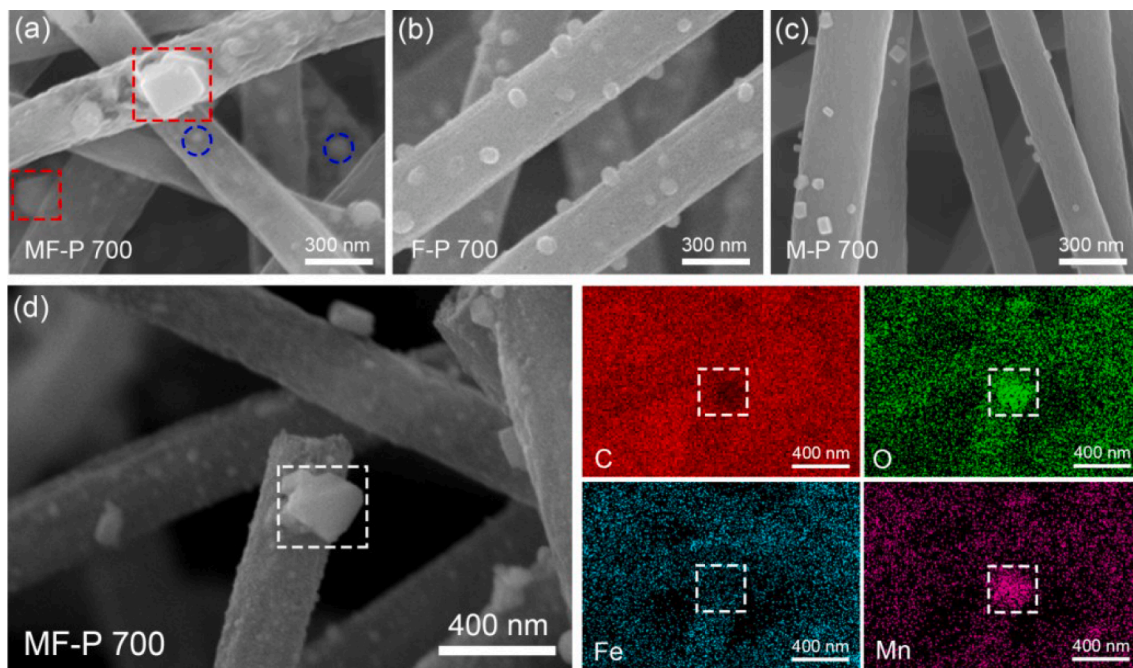


Fig. 5. FE-SEM images of (a) MF-P 700, (b) F-P 700, (c) M-P 700. (d) FE-SEM images of MF-P 700 and its elemental mapping images related to C, O, Fe and Mn.

quantitative analysis of its XRD pattern. Only the peaks of MnO and Fe₃C are found in XRD pattern of MF-P 800, meaning that Fe₃O₄ formed at low annealing temperatures is reduced into Fe₃C by carbon and MnO

remains unchanged at 800 °C. The mass ratio of MnO and Fe₃C in MF-P 800 is determined to be 1:2 from quantitative analysis of its XRD pattern.

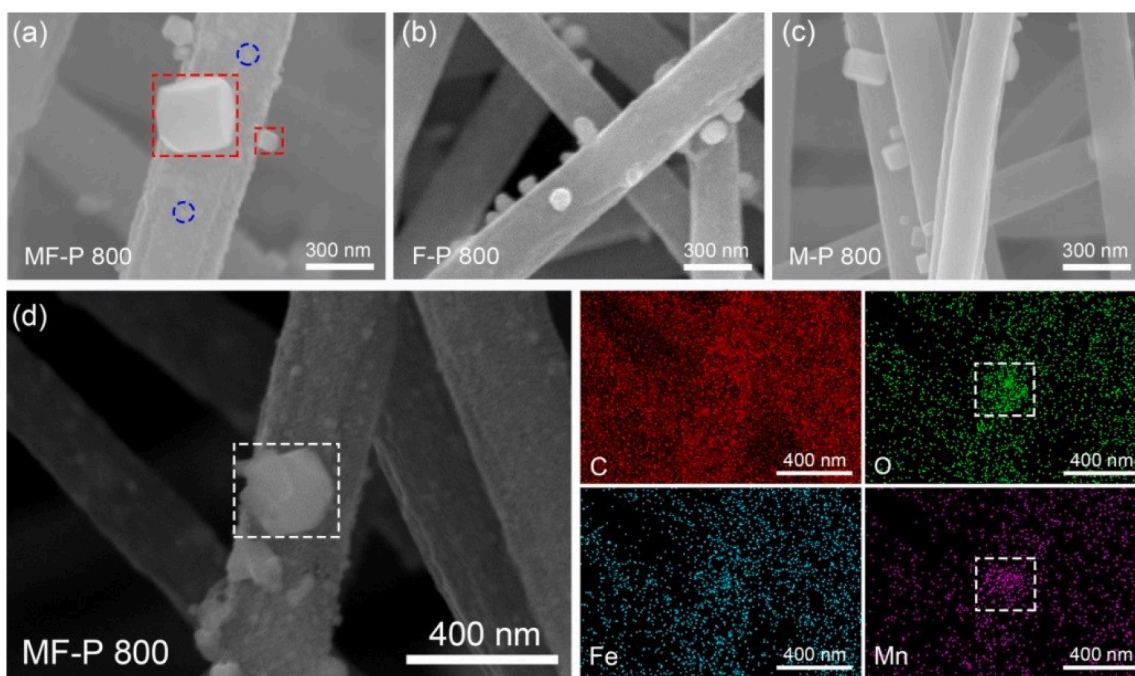


Fig. 6. FE-SEM images of (a) MF-P 800, (b) F-P 800, (c) M-P 800. (d) FE-SEM images of MF-P 800 and its elemental mapping images related to C, O, Fe and Mn.

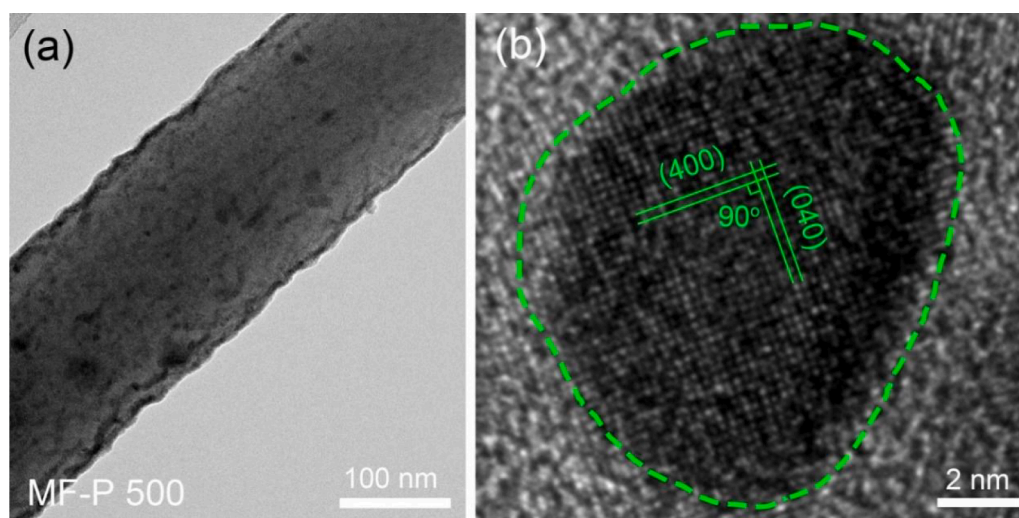


Fig. 7. Typical BF TEM (a) and HRTEM (b) images of MF-P 500.

Fig. 2 displays typical low and high magnification FE-SEM images of MF-P fiber membranes. From the low-magnification FE-SEM images (Fig. 2a, c, e, g and i) of MF-P 400, MF-P 500, MF-P 600, MF-P 700 and MF-P 800, it can be seen that fibers are well dispersed and have relatively uniform diameters. The enlarged SEM images of MF-P 400, MF-P 500, MF-P 600, MF-P 700 and MF-P 800 are presented in Fig. 2b, d, f, h and j, respectively. In MF-P 400, the fibers have a quite smooth surface caused by the poor crystallization of Fe_3O_4 at 400 °C. In MF-P 500, many spherical nanoparticles are observed in the fibers and the number of nanoparticles increases greatly in MF-P 600. This is attributed to the further crystallization of nanoparticles and their diffusion from inside to the surface of fibers. For the MF-P 700, the diameter of the spherical particles becomes larger and some cuboidal particles appear on the surface of fibers. Compared to MF-P 700, MF-P 800 has more cuboidal particles and some pores are found on the surface which may be due to the falling-off of the formed nanoparticles. As shown in Fig. 2, the fiber

diameter decreases as the annealing temperature increases. The statistical analysis in Fig. 3 illustrated the reduction of average diameter more clearly, which is ascribed to the release of more gases at higher annealing temperatures [22,23].

To analyze the composition of elements of the sample, EDS spectra were performed. Fig. 4(a–d) show the EDS spectra of MF-P 500, MF-P 600, MF-P 700 and MF-P 800, respectively, in which the tables display the mass ratio of the elements in the samples. The peaks not marked in the spectra are caused by gold plating. The quantification results of EDS spectra are consistent with those of XRD patterns. To distinguish the spherical and cuboidal nanoparticles on the fiber surface, the morphologies of the carbon fibers loaded with iron compounds (F-P 700 and F-P 800) and manganese compounds (M-P 700 and M-P 800) were investigated, which are presented in Figs. 5 and 6. Both cuboidal particles (marked by red rectangle) and spherical particles (marked by blue circles) can be found in MF-P 700 and MF-P 800. However, only

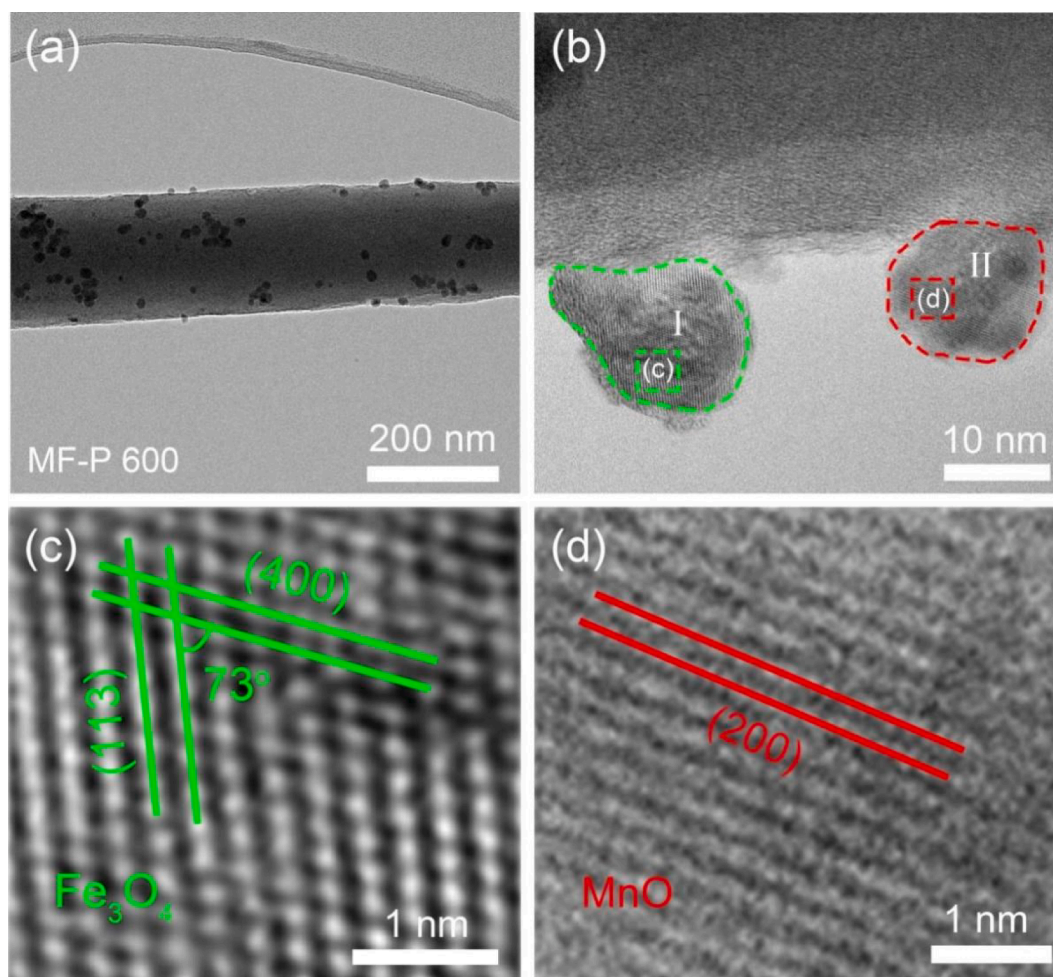


Fig. 8. Typical BF TEM (a) and HRTEM (b) images of MF-P 600. HRTEM image of the area surrounded by the green square(c) and the area surrounded by the red square(d) in (b).

spherical nanoparticles exist in F-P 700 and F-P 800 while cuboidal particles are found in M-P 700 and M-P 800. Thus, it is deduced that the spherical particles are iron compounds, while the cuboidal particles are made up of manganese compounds. The elemental mapping examination was performed to further verify the composition of the cuboidal nanoparticles. Figs. 5d and 6d show the elements distribution of the cuboidal nanoparticles in MF-P 700 and MF-P 800, respectively. It can be seen that these particles (enveloped by white rectangles) are made up of O and Mn elements. Based on XRD analysis and elemental mapping results, the cuboidal particles are determined to be MnO.

To further investigate the phase evolution process at different annealing temperatures, extensive TEM characterizations were carried out. Fig. 7a shows BF TEM image of MF-P 500. There are few nanoparticles embed in the fiber's surface, which is consistent with our SEM result. Fig. 7b displays the HRTEM image of MF-P 500. The interplanar spacing is measured to be 2.10 Å and the angle between the two planes is 90°, corresponding to the {400} planes of Fe₃O₄, which demonstrates that the Fe₃O₄ nanocrystals were produced at 500 °C. From the enlarged TEM image of MF-P 600 shown in Fig. 8b, two different particles can be observed, which are named as particle I and II, respectively. The HRTEM images in Fig. 8c and d are obtained from the rectangular regions in particle I and II, respectively. In particle I, the interplanar spacings are 2.53 Å and 2.10 Å by carefully measured, corresponding to the (311) and (400) crystal planes of Fe₃O₄, respectively. The angle is determined to be 73°, consistent with the theoretical value of Fe₃O₄. In particle II, the lattice spacing in the HRTEM image is measured to be 2.22 Å, in

accordance with the (200) crystal plane of MnO. Therefore, both Fe₃O₄ and MnO exist in the carbon fibers of MF-P 600. Fig. 9a and b are the BF TEM and HRTEM images of MF-P 700, respectively. The enlarged HRTEM images indicate that the particles labeled by the red, yellow, and green lines in Fig. 9b correspond to MnO, Fe₃C and Fe₃O₄, respectively. Fig. 9c shows the enlarged HRTEM images of particle I in Fig. 9b, which is determined to be MnO according to the measured interplanar spacings. Fig. 9d and e demonstrate the enlarged HRTEM images of particle II and III in Fig. 9b, respectively. All of them are determined to be Fe₃C by measuring the interplanar spacings and the angle between two planes. Fig. 9f is the enlarged images of particle IV in Fig. 9b. It can be confirmed as Fe₃O₄ by measuring its planar spacing. HRTEM examination of MF-P 700 demonstrates that when the annealing temperature reaches 700 °C, part of Fe₃O₄ is reduced into Fe₃C while MnO remains unchanged, which is in good agreement with the XRD results. From the HRTEM image of MF-P 800 in Fig. 10b, only MnO and Fe₃C nanoparticles, enclosed by the red and yellow lines, are observed, indicating that the Fe₃O₄ is completely reduced by carbon at 800 °C.

To further explore the decomposition temperature of Mn(acac)₃/Fe(acac)₃/PAN fibers (MF-P), thermogravimetric analysis (TGA) was conducted. First, the temperature increases from 30 °C up to 230 °C with a heating rate of 10 °C/min in air atmosphere. After kept in air for 2 h, the temperature is continually increased to 900 °C with a heating rate of 10 °C/min in Ar atmosphere. Fig. 11 is the TGA curves obtained from pure PAN fibers (P) and PAN fibers loaded with Mn(acac)₃/Fe(acac)₃. It can be clearly seen that the weight of both samples changes slowly in the

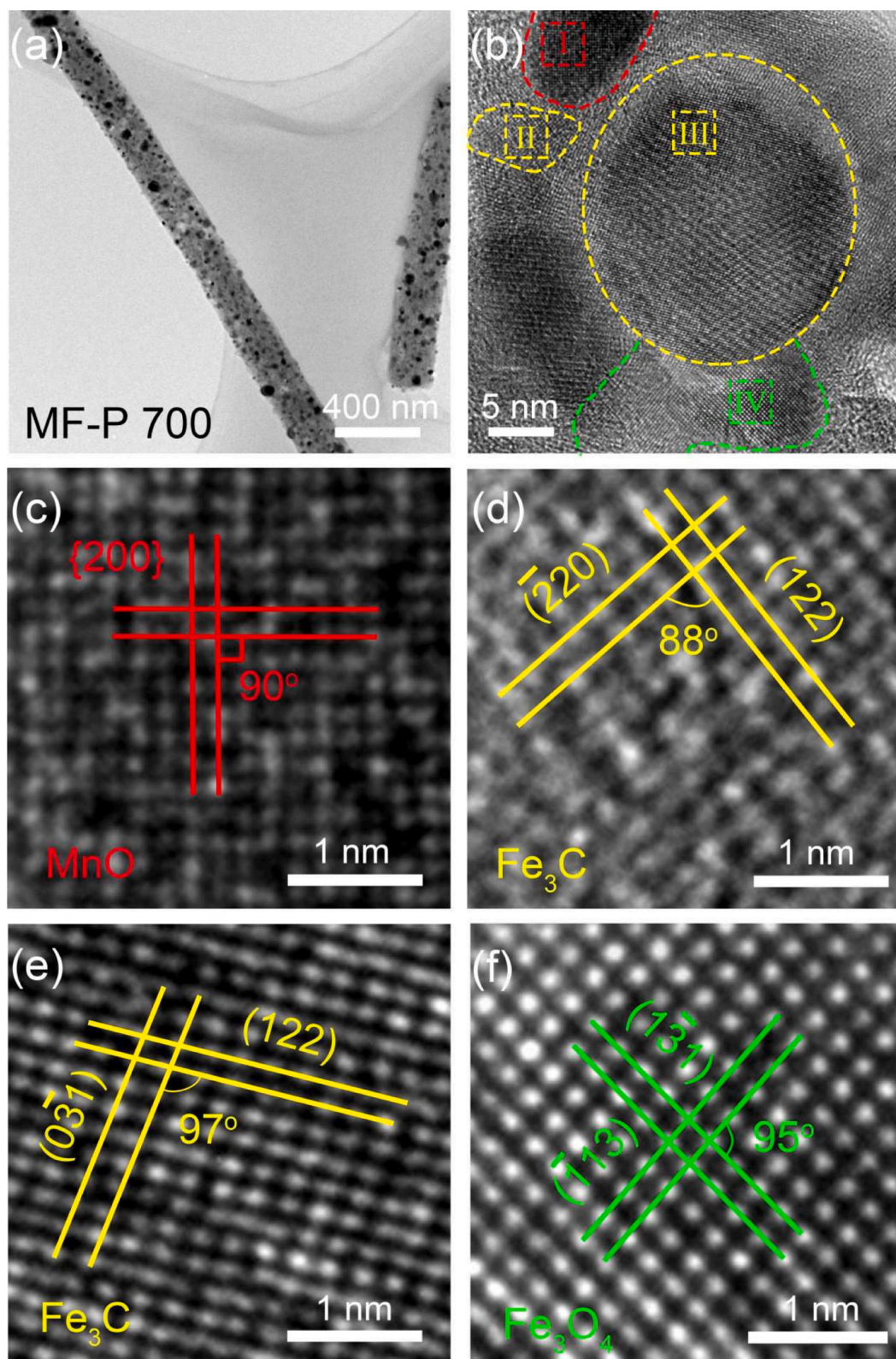


Fig. 9. Typical BF TEM (a) and HRTEM (b) images of MF-P 700. HRTEM image of the area surrounded by the square I(c), II(d), III(e) and IV(f) in (b).

temperature range from 30 °C to 160 °C, corresponding to the volatilization of moisture and solvent in the sample. The decomposition of $\text{Mn}(\text{acac})_3/\text{Fe}(\text{acac})_3$ is presented by the sharp decline of MF-P in the temperature range of 160 °C (A)–230 °C. The TGA curve of MF-P is parallel to that of P in the temperature range from B to C, indicating that

formation of Fe_3O_4 occurs in the temperature range of 360–598 °C. The weight of MF-P decreases drastically in the temperature range of 598–710 °C (C-D), which corresponds to the formation of MnO and transformation from Fe_3O_4 to Fe_3C , confirmed by the XRD and TEM analyses.

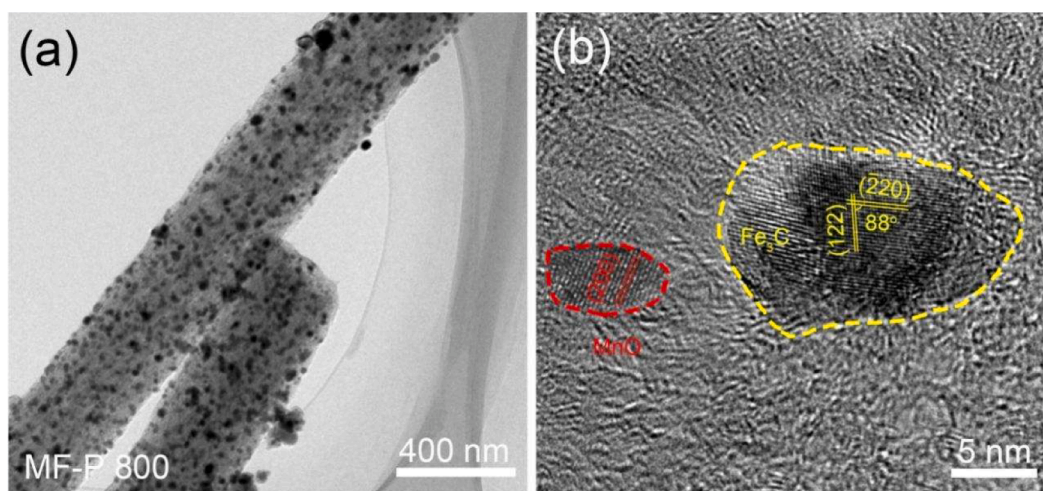


Fig. 10. Typical BF TEM (a) and HRTEM (b) images of MF-P 800.

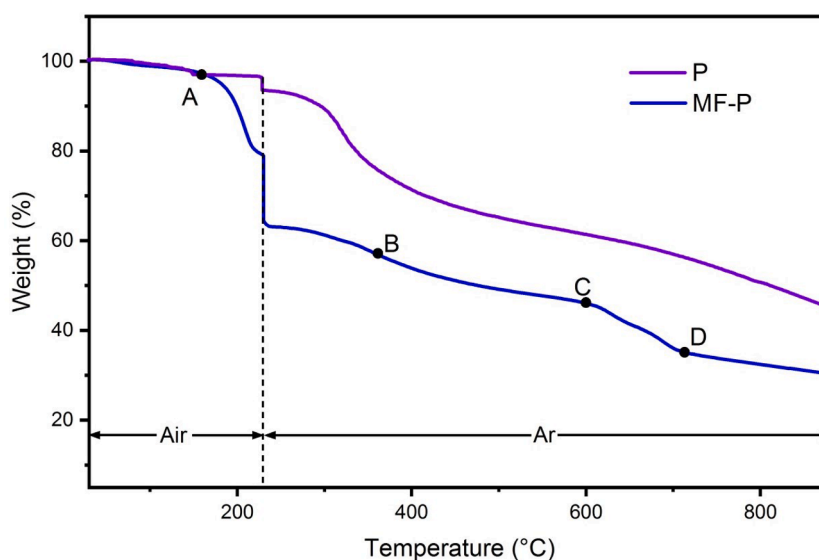


Fig. 11. TGA curves of $\text{Mn}(\text{acac})_3/\text{Fe}(\text{acac})_3$ -PAN fibers (MF-P) and PAN fibers (P).

Fig. 12 shows the XPS spectra obtained from MF-P 500–800. Fig. 12b and e display typical spectra of Fe_3O_4 with two peaks located at 710 eV and 724 eV, corresponding to $\text{Fe } 2p_{3/2}$ and $\text{Fe } 2p_{1/2}$, respectively. [24, 25] The $\text{Fe } 2p_{3/2}$ spectrum consists of two single peaks corresponding to Fe^{2+} (710 eV) and Fe^{3+} (712 eV), respectively. The $\text{Fe } 2p_{1/2}$ spectrum shows characteristic of Fe^{2+} (723 eV) and Fe^{3+} (726 eV). [26] The $\text{Fe } 2p$ peak positions and splittings vary for different samples due to different valences of Fe. [27] When the temperature reaches 700 °C, apart from typical spectra of Fe_3O_4 , two peaks are also found at 707 eV and 722 eV, corresponding to $2p_{3/2}$ and $2p_{1/2}$ of Fe_3C . [28] This further confirms that Fe_3O_4 and Fe_3C co-exist at 700 °C. In Fig. 12k, two peaks are found at 707 eV and 722 eV, corresponding to $2p_{3/2}$ and $2p_{1/2}$ of Fe_3C . The other four peaks located at 710, 712, 723 and 726 eV result from surface oxidation. [29] The peaks at 716, 720, 728 and 733 eV are satellite peaks of $\text{Fe } 2p$. Fig. 12c, f, i and l show typical spectra of MnO with appearance of two peaks at 653 and 642 eV, corresponding to $\text{Mn } 2p_{1/2}$ and $\text{Mn } 2p_{3/2}$, respectively. [30]

Based on the XRD and HRTEM results, we propose a phase evolution mechanism of the iron and manganese compounds in carbon fibers, as shown in Fig. 13. While the annealing temperature reaches 500 °C, only Fe_3O_4 nanoparticles are produced in carbon fibers. As the temperature rises to 600 °C, MnO nanoparticles begin to form. With further increasing temperature, Fe_3O_4 is gradually reduced by carbon and transforms into Fe_3C , and this process continues until the annealing temperature reaches 800 °C. However, MnO remains unchanged in the reductive carbon environment during the whole annealing process, which is ascribed to the low valence state of manganese. Therefore, both Fe_3C and MnO are found in MF-P 800.

The electrochemical performances of MF-P samples as anode materials are systematically investigated. Fig. 14a–d display the initial five CV curves obtained at a specific scanning rate of 0.3 mV s^{-1} of MF-P 500, MF-P 600, MF-P 700 and MF-P 800 electrodes, respectively. For the MF-P 500 electrode, only a reduction peak is observed at 0.25 V in the first cathodic scan, which is attributed to the irreversible formation process

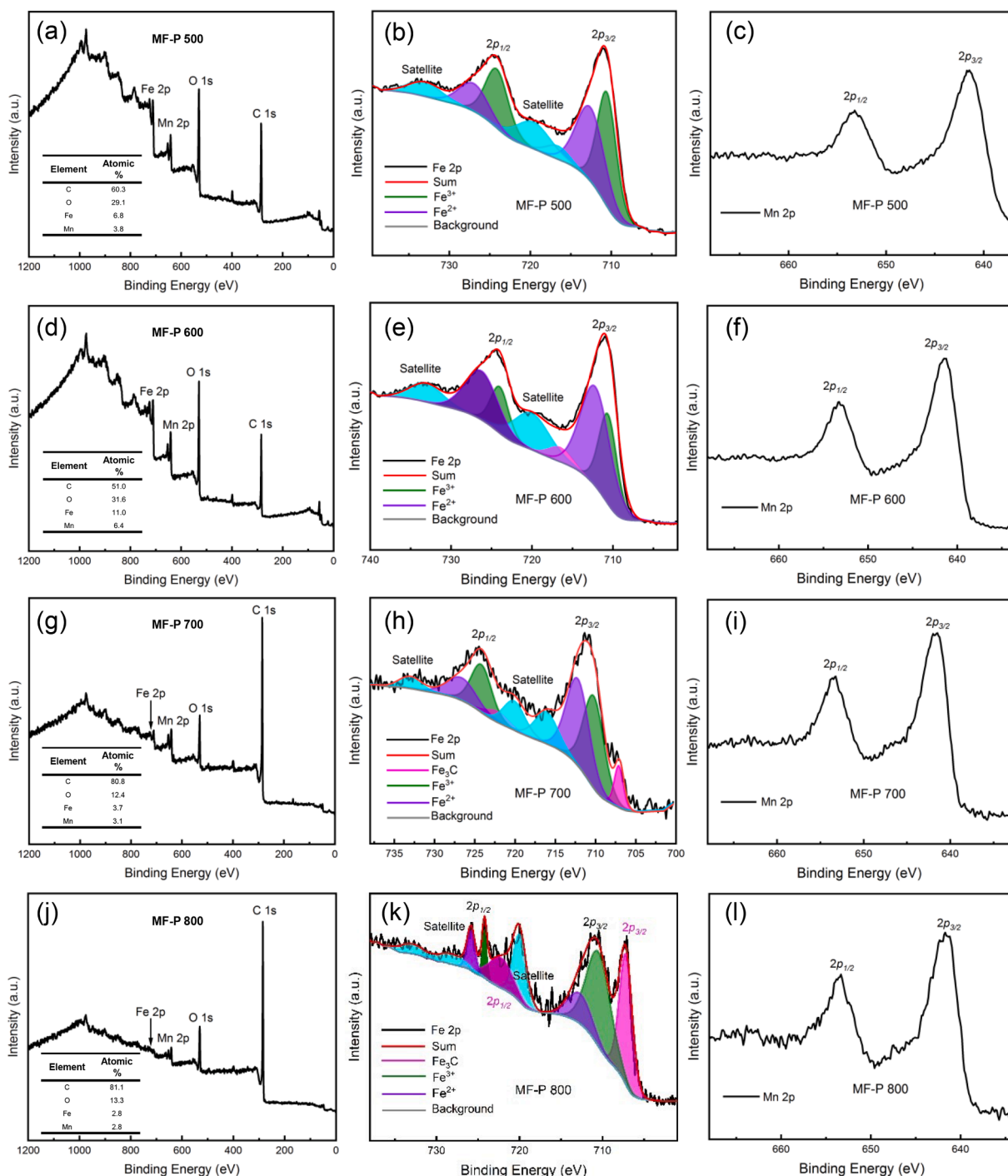


Fig. 12. Full-scan XPS spectra (a, d, g, j) of MF-P 500, MF-P 600, MF-P 700 and MF-P 800; High-resolution spectra of Fe 2p (b, e, h, k) and Mn 2p (c, f, i, l).

of solid electrolyte interface (SEI) film on the electrode surface. No obvious redox peaks are found in the following cycles due to the low crystallinity of active materials in MF-P 500. Fig. 14b shows the CV curves of MF-P 600, which is similar to the typical CV curve of Fe_3O_4 with sharp reduction peaks at ~ 0.5 V and weak oxidation peaks at ~ 1.2 V, corresponding to the insertion and extraction of lithium ions in Fe_3O_4 , respectively. However, the peak at 0.41 V in the first cathodic scanning here is slightly lower than the reported potentials (0.5 V) for Fe_3O_4 [31] but close to that of FeO (0.39 V) [32]. In addition, the initial reduction potentials of both MF-P 700 (0.34 V) and MF-P 800 (0.31 V) are higher than the reported potentials (0.1 V) for MnO [33]. The shifts

of the first cathodic peaks may be attributed to the oxidation of Mn-based compound by Fe-based compounds. The subtle reduction peaks in the first scanning process of MF-P 800 electrodes at 0.69 V and 1.51 V correspond to the insertion process of lithium ion into Fe_3C [34]. The weak anodic peaks of MF-P 700 and MF-P 800 at about 1.29 V are mainly associated with the delithiation process of MnO and Fe_3C . In the subsequent cycle, both reduction and oxidation peaks in Fig. 14b–d shift towards high voltage, which are ascribed to the polarization of the active materials and the formation of irreversible SEI film during the electrochemical cycle [35]. All the aforementioned electrochemical reactions belong to conversion reactions because the no alloy forms during

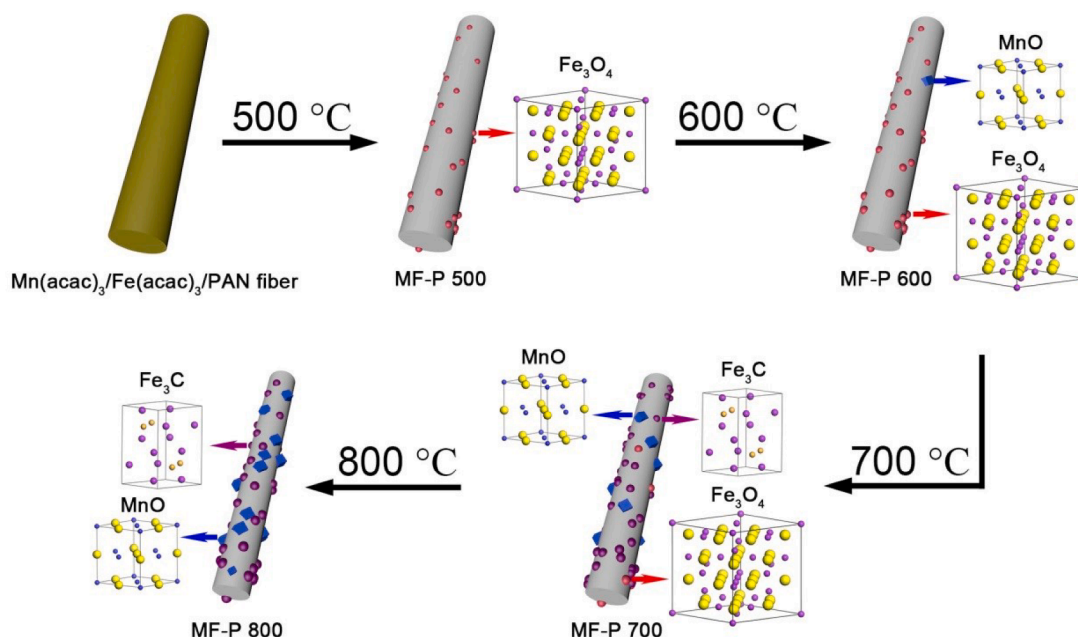


Fig. 13. Phase evolution process during annealing process.

the charge and discharge process. For Fe_3O_4 and MnO components, the electrochemical reactions only involve the formation and decomposition of Li_2O , as well as the reduction and oxidation of metal nanoparticles, which is typical for conversion reactions. [36] For Fe_3C component, although cubic iron is produced during cycling process, it does not alloy with Li because of their relatively high electronegativity difference (0.85) and unmatched valence state (+3 vs. +1) according to the Hume-Rothery rules. [34] Fig. 14e–h illustrate the initial five discharge/charge profiles of MF-P 500, MF-P 600, MF-P 700 and MF-P 800 electrodes at a fixed current density of 0.2 A g^{-1} . The evident discharge potential plateaus of the four samples agree well with their cathodic peaks in the corresponding CV curves. The initial discharge capacities of MF-P 500, MF-P 600, MF-P 700 and MF-P 800 electrodes are 695.9, 728.7, 1196.3 and 449.1 mAh g^{-1} , respectively. MF-P 700 electrode exhibits the highest capacity, as a result of the synergistic effect of Fe_3O_4 , MnO and Fe_3C .

To further investigate the electrochemical performance of MF-P samples, the rate performance and cycling stability were examined. As displayed in Fig. 15a, the rate performance of four electrodes is tested under different current densities. MF-P 700 electrode presents the optimal rate performance with the average specific discharge capacity of $719.25 \text{ mAh g}^{-1}$, $638.95 \text{ mAh g}^{-1}$, $575.45 \text{ mAh g}^{-1}$, $486.17 \text{ mAh g}^{-1}$ and 361.4 mAh g^{-1} at current densities of 0.1, 0.2, 0.5, 1 and 2 A g^{-1} , respectively. The specific capacity ($762.59 \text{ mAh g}^{-1}$) is higher than its initial value ($719.25 \text{ mAh g}^{-1}$) as the current density returns to 0.1 A g^{-1} , indicating that the electrode materials can be effectively activated by higher current density during charge/discharge cycle [37]. The theoretical specific capacity of each anode and the C-rates under different current densities are displayed in Table 1. Fig. 15b displays the electrochemical cycling performance of MF-P electrodes under a fixed current density of 0.2 A g^{-1} . After 250 cycles, the specific discharge capacities of MF-P 500, MF-P 600, MF-P 700 and MF-P 800 electrodes are 510.1 mAh g^{-1} , 542.5 mAh g^{-1} , $750.23 \text{ mAh g}^{-1}$ and 223.2 mAh

g^{-1} , respectively. For all the electrodes, the specific capacity gradually increases with increasing cycle number because the active substances are gradually activated with increasing cycle time. This phenomenon is common in half cell tests when the metal oxides are used as anode material [38–40]. By comparison, the MF-P 700 electrode exhibits the best cyclic stability. The improved rate and cycling performances of MF-P 700 electrode are attributed to the following three reasons: Firstly, the mixture of Fe_3O_4 and MnO in carbon fibers has higher theoretical specific capacity, which is conducive to storing more lithium ions. Secondly, the appearance of MnO improves the cyclic stability of iron compounds. Thirdly, the formation of SEI film has been partially suppressed due to the outstanding catalytic activity of Fe_3C , leading to the increase of specific capacity [41,42]. The mass, thickness and areal current of each anode, together with the components and their contribution to specific capacity of each anode were displayed in Table 2.

To study the electrochemical reaction kinetics of MF-P electrodes, EIS tests were performed. As shown in Fig. 15c, all four EIS spectrum consist of two parts: a semicircle and an inclined line in the regions of high frequency and low frequency, respectively. The illustration in Fig. 15c is the corresponding circuit diagram of the electrode. The fitting parameters used in the equivalent circuit are summarized in Table 3. The electrolyte impedance, charge transfer impedance, Warburg impedance and double-layer capacitance are denoted as R_s , R_{ct} , W and CPE , respectively [43]. With the increase of annealing temperature, the semicircle diameter decreases gradually, demonstrating that MF-P samples obtained at higher annealing temperature exhibit the lower charge transfer impedance. The R_{ct} s of MF-P 500, MF-P 600, MF-P 700 and MF-P 800 electrodes are 474Ω , 205Ω , 200Ω and 147Ω , respectively, demonstrating that the charge transfer impedance of the obtained electrode can be reduced by increasing the temperature during annealing procedure [44]. The inclined line in low frequency region is related to the Li^+ diffusion of the electrode [45] and the diffusion coefficient of lithium ions (D_{Li}) can be calculated by the following equations [46].

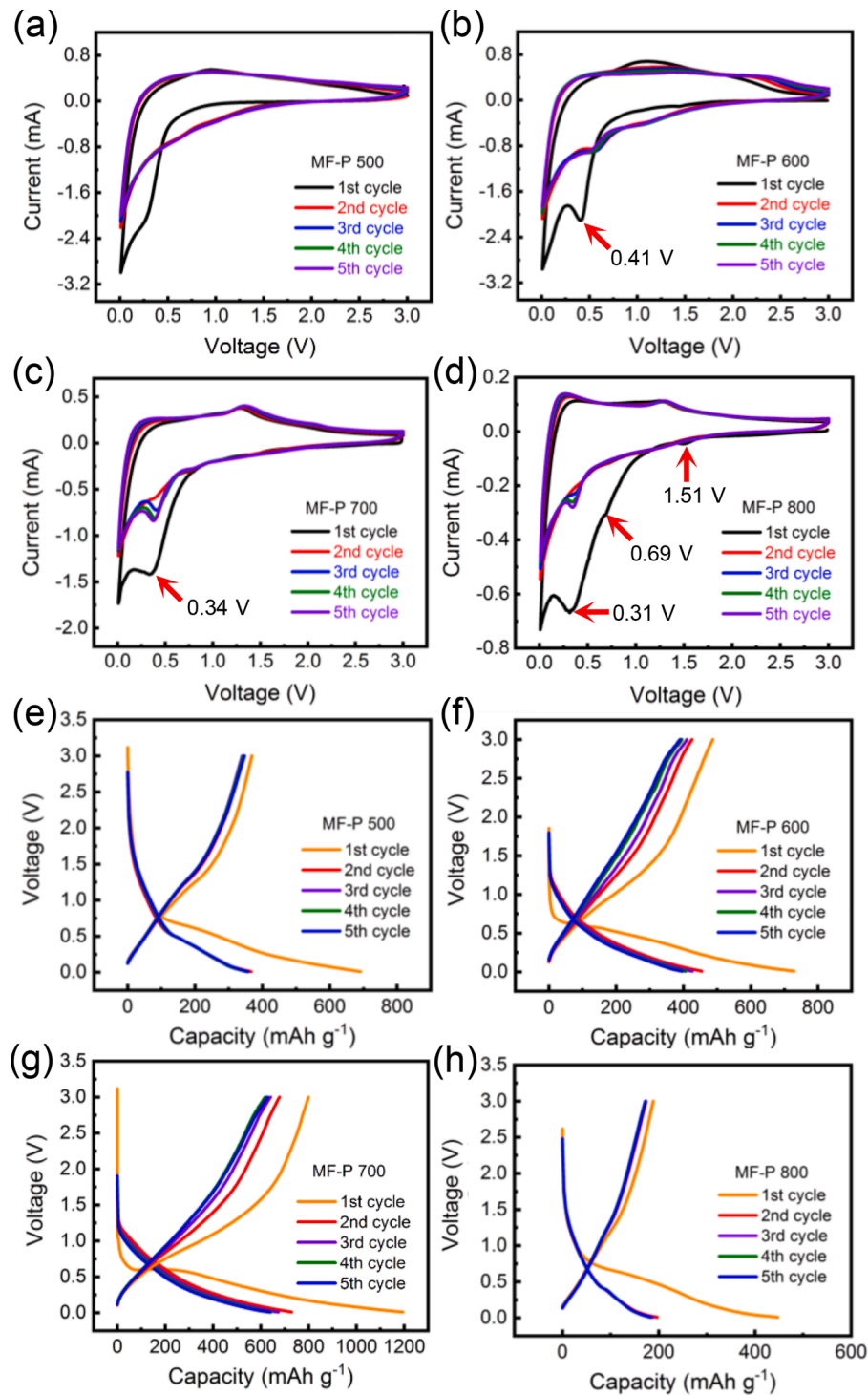


Fig. 14. CV curves of MF-P 500 (a), MF-P 600 (b), MF-P 700 (c), and MF-P 800 (d) obtained at 0.3 mV s^{-1} . Initial voltage versus capacity curves of MF-P 500 (e), MF-P 600 (f), MF-P 700 (g), and MF-P 800 (h) electrodes at a current density of 0.2 A g^{-1} .

$$D_{\text{Li}} = \frac{R^2 T^2}{2A^2 n^4 F^4 C^2 \sigma^2} \quad (1)$$

$$Z' = R_s + R_{ct} + \sigma \omega^{-0.5} \quad (2)$$

where the constant values of Faraday is $96,485 \text{ C mol}^{-1}$, denoted as F . The gas constant R is $8.314 \text{ J K}^{-1} \text{ mol}^{-1}$. The electrode area A is $1.54 \times 10^{-4} \text{ m}^2$. T is 298.15 K . n is the number of the electrons of single molecule participating in the electron transfer reaction, and C represents

the Li^+ concentration of the electrode. The σ values (slope of the line) of MF-P 500, MF-P 600, MF-P 700 and MF-P 800 are 1270.9 , 426.1 , 154.9 and $39.1 \text{ } \Omega \text{ s}^{-0.5}$, respectively. The D_{Li} of MF-P 500, MF-P 600, MF-P 700 and MF-P 800 electrodes are 4.5×10^{-27} , 3.9×10^{-26} , 2.9×10^{-25} and $4.7 \times 10^{-24} \text{ cm}^2 \text{ s}^{-1}$, respectively, demonstrating that the electrode obtained at higher annealing temperature has higher Li^+ diffusion coefficient. This is attributed the fact that the diameter of the carbon fiber gradually decreases with the increase of annealing temperature, leading to the shortening of Li^+ diffusion distance [47]. In a word, the charge

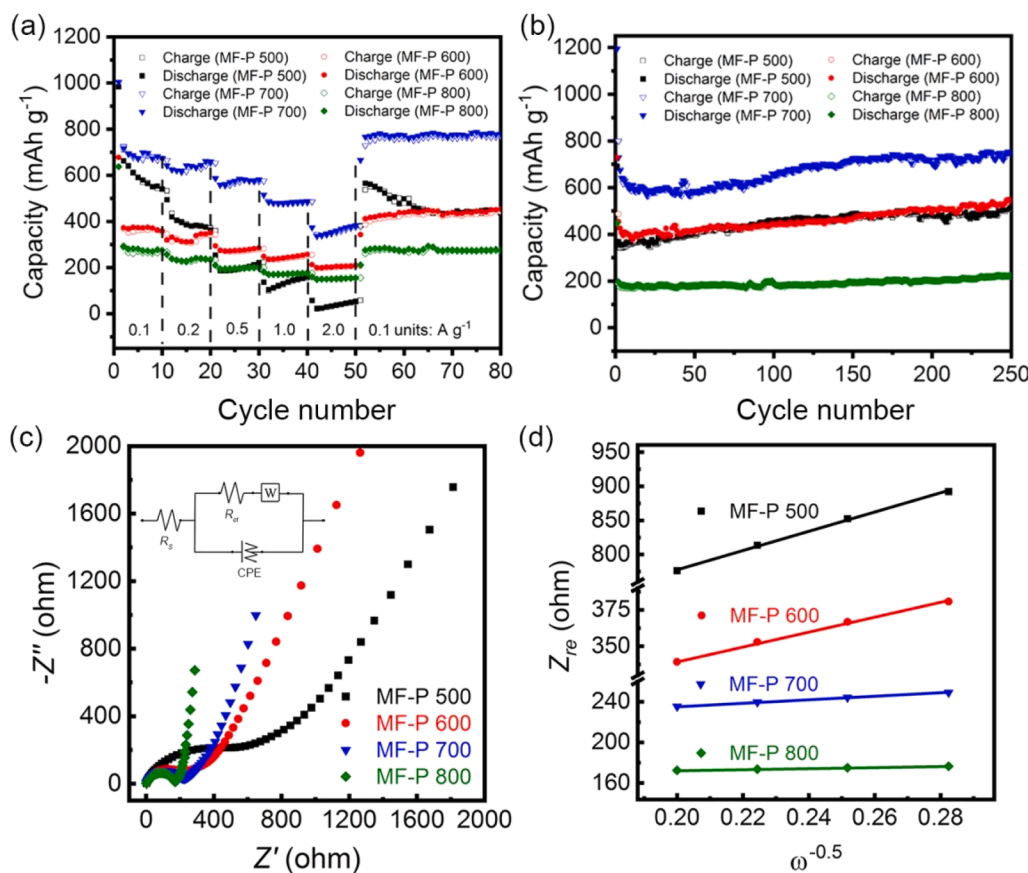


Fig. 15. Rate performance at various current densities (a), cycling performance at 200 mA g⁻¹ (b), EIS spectra (c) and Graph of Z_{re} plotted against $\omega^{-0.5}$ (d) of MF-P 500, MF-P 600, MF-P 700, and MF-P 800 electrodes. The inset in (c) shows the equivalent circuit used for fitting impedance spectra.

transfer impedance of MF-P samples can be effectively decreased by increasing the annealing temperature thus possessing higher Li⁺ diffusion ability.

4. Conclusions and perspectives

In conclusion, the heterogeneous flexible anode materials with different Fe/Mn-based nanoparticles embedded in carbon fibers were fabricated by electrospinning technique under various annealing temperatures. Different composites, Fe₃O₄/CF, Fe₃O₄/MnO/CF, Fe₃O₄/Fe₃C/MnO/CF and Fe₃C/MnO/CF, are obtained at 500, 600, 700 and 800 °C, respectively. Among four electrodes, Fe₃O₄/Fe₃C/MnO/CF exhibits excellent specific capacity (750.23 mAh g⁻¹ after 250 cycles), which results from the higher specific capacity of the mixed oxides (MnO and Fe₃O₄) as well as the catalytic activation and good conductivity of Fe₃C. In addition, the excellent cycling stability of Fe₃O₄/Fe₃C/MnO/CF during charge/discharge process is attributed to the carbon coating and mixing with manganese oxides. Our work will help deepen the understanding of the phase transition of Fe/Mn-based compounds in carbon fibers and the relationship between phase constituent and lithium-storage performance.

CRediT authorship contribution statement

Fei Xie: Investigation, Formal analysis, Writing – original draft. **Xiaoli Sheng:** Conceptualization, Investigation, Formal analysis. **Zhibin Ling:** Formal analysis, Writing – review & editing. **Shujin Hao:** Formal analysis, Validation, Methodology. **Qingye Zhang:** Formal analysis, Validation. **Meng Sun:** Formal analysis, Validation. **Guanting Liu:** Formal analysis, Validation. **Feiyu Diao:** Formal analysis, Methodology, Writing – review & editing. **Yiqian Wang:** Conceptualization, Funding acquisition, Supervision, Writing – review & editing.

Declaration of Competing Interest

There are no conflicts to declare.

Data availability

Data will be made available on request.

Table 1

The theoretical specific capacity of each anode and its C-rate under different current density.

Anode	Theoretical specific capacity (mAh g ⁻¹)	Current density (mA g ⁻¹)	C-rate
MF-P 500	460.6	0.1	0.22 C
		0.2	0.44 C
		0.5	1.10 C
		1.0	2.20 C
		2.0	4.40 C
MF-P 600	552.0	0.1	0.18 C
		0.2	0.36 C
		0.5	0.90 C
		1.0	1.80 C
		2.0	3.60 C
		0.1	0.3 C
MF-P 700	339.0	0.2	0.6 C
		0.5	1.50 C
		1.0	3.0 C
		2.0	6.0 C
		0.1	0.34 C
MF-P 800	292.0	0.2	0.68 C
		0.5	1.70 C
		1.0	3.40 C
		2.0	6.80 C
		0.1	0.34 C
		0.2	0.68 C

Table 2

The mass, thickness and areal current of each anode, together with the components and their contribution to specific capacity of each anode.

Anode	Mass (mg)	Thickness (μm)	Areal current (mAh cm ⁻²)	Component	Specific capacity (mAh g ⁻¹)	Component contribution
MF-P 500	2.2	204.0	0.73	C	346.0	67.8 %
				Fe ₃ O ₄	164.1	32.2 %
MF-P 600	2.1	202.0	0.74	C	229.8	42.4 %
				Fe ₃ O ₄	201.2	37.1 %
				MnO	111.5	20.5 %
MF-P 700	2.0	200.0	0.97	C	390.5	52.0 %
				Fe ₃ O ₄	104.9	14.0 %
				MnO	236.8	31.6 %
				Fe ₃ C	18.0	2.4 %
MF-P 800	1.9	198.0	0.28	C	109.4	49.0 %
				MnO	105.4	3.8 %
				Fe ₃ C	8.4	47.2 %

Table 3The electrolyte impedance R_s , charge transfer impedance R_{ct} , Warburg impedance W and double-layer capacitance CPE of MF-P 500, MF-P 600, MF-P 700 and MF-P 800 electrodes.

Anode materials	R_s (Ω)	R_{ct} (Ω)	W (mMho)	CPE (μMho)
MF-P 500	2.6	474.0	1.4	11.7
MF-P 600	3.4	205.0	1.7	14.3
MF-P 700	1.6	200.0	1.9	14.7
MF-P 800	1.8	147.0	2.3	9.6

Acknowledgments

The authors would like to thank the financial support from High-end foreign experts project of the Ministry of Science and Technology, China (Grant no.: G2022025015L, G2022025016L), the Shandong Province "Double-Hundred Talent Plan" (Grant No.: WST2018006), and the Top-notch Innovative Talent Program of Qingdao City, China (Grant no.: 13-CX-8). Y. Q. Wang would also like to thank the financial support from the Taishan Scholar Program of Shandong Province, China, Qingdao International Center of Semiconductor Photoelectric Nanomaterials, and Shandong Provincial University Key Laboratory of Optoelectrical Material Physics and Devices.

References

- [1] X.W. Ma, M.Y. Zhang, C.Y. Liang, Y.S. Li, J.J. Wu, R.C. Che, Inheritance of crystallographic orientation during lithiation/delithiation processes of single-crystal α -Fe₂O₃ nanocubes in lithium-ion batteries, *ACS Appl. Mater. Interfaces* 7 (2015) 24191–24196.
- [2] S.K. Jung, I. Hwang, S.P. Cho, K. Oh, K. Ku, I.R. Choi, K. Kang, New iron-based intercalation host for lithium-ion batteries, *Chem. Mater.* 30 (2018) 1956–1964.
- [3] X. Hua, P.K. Allan, C. Gong, P.A. Chater, E.M. Schmidt, H.S. Geddes, A. W. Robertson, P.G. Bruce, A.L. Goodwin, Non-equilibrium metal oxides via reconversion chemistry in lithium-ion batteries, *Nat. Commun.* 12 (2021) 561.
- [4] H.J. Chen, X.D. Ma, P.K. Shen, *In-situ* encapsulating FeS/Fe₃C nanoparticles into nitrogen-sulfur dual-doped graphene networks for high-rate and ultra-stable lithium storage, *J. Alloy. Compd.* 779 (2019) 193–201.
- [5] D.W. Jung, J.H. Jeong, S.W. Han, E.S. Oh, Electrochemical performance of potassium-doped wustite nanoparticles supported on graphene as an anode material for lithium ion batteries, *J. Power Sources* 315 (2016) 16–22.
- [6] M.X. Gao, P. Zhou, P. Wang, J.H. Wang, C. Liang, J.L. Zhang, Y.F. Liu, FeO/C anode materials of high capacity and cycle stability for lithium-ion batteries synthesized by carbothermal reduction, *J. Alloy. Compd.* 565 (2013) 97–103.
- [7] X.Y. Zhao, D.G. Xia, J.C. Yue, S.Z. Liu, *In-situ* generated nano-Fe₃C embedded into nitrogen-doped carbon for high performance anode in lithium ion battery, *Electrochim. Acta* 116 (2014) 292–299.
- [8] X.L. Wang, Y.G. Liu, H.Y. Han, Y.Y. Zhao, W.M. Ma, H.Y. Sun, Polyaniline coated Fe₃O₄ hollow nanospheres as anode materials for lithium ion batteries, *Sustain. Energy Fuels* 1 (2017) 915–922.
- [9] Y.Q. Fu, Q.L. Wei, X.Y. Wang, G.X. Zhang, H.B. Shu, X.K. Yang, A.C. Tavares, S. H. Sun, A facile synthesis of Fe₃O₄ nanoparticles/graphene for high-performance lithium/sodium-ion batteries, *RSC Adv.* 6 (2016) 16624–16633.
- [10] X.J. Wang, X.J. Liu, G. Wang, Y. Xia, H. Wang, One-dimensional hybrid nanocomposite of high-density monodispersed Fe₃O₄ nanoparticles and carbon nanotubes for high-capacity storage of lithium and sodium, *J. Mater. Chem. A* 4 (2016) 18532–18542.
- [11] Y. Wang, X.M. Guo, Z.K. Wang, M.F. Lu, B. Wu, Y. Wang, C. Yan, A.H. Yuan, H. X. Yang, Controlled pyrolysis of MIL-88A to Fe₂O₃@C nanocomposites with varied morphologies and phases for advanced lithium storage, *J. Mater. Chem. A* 5 (2017) 25562–25573.
- [12] M.Z. Zou, L.L. Wang, J.X. Li, L.H. Guan, Z.G. Huang, Enhanced Li-ion battery performances of yolk-shell Fe₃O₄@C anodes with Fe₃C catalyst, *Electrochim. Acta* 233 (2017) 85–91.

- [13] T.T. Ma, Y.S. Xu, L. Sun, X.H. Liu, J. Zhang, Synthesis of graphene/ α -Fe₂O₃ nanospindles by hydrothermal assembly and their lithium storage performance, *Ceram. Int.* 44 (2018) 364–368.
- [14] R.O. Chavez, T.P. Lodge, M. Alcoutlabi, Recent developments in centrifugally spun composite fibers and their performance as anode materials for lithium-ion and sodium-ion batteries, *Mater. Sci. Eng. B* 266 (2021), 115024.
- [15] L. Zuniga, G. Gonzalez, R.O. Chavez, J.C. Myers, T.P. Lodge, M. Alcoutlabi, Centrifugally spun α -Fe₂O₃/TiO₂/carbon composite fibers as anode materials for lithium-ion batteries, *Appl. Sci.* 9 (2019) 4032.
- [16] V.A. Agubra, L. Zuniga, D. Flores, H. Campos, J. Villarreal, M. Alcoutlabi, A comparative study on the performance of binary SnO₂/NiO/C and Sn/C composite nanofibers as alternative anode materials for lithium ion batteries, *Electrochim. Acta* 224 (2017) 608–621.
- [17] J.G. Wang, H.Y. Liu, H.Z. Liu, Z.H. Fu, D. Nan, Facile synthesis of microsized MnO/C composites with high tap density as high performance anodes for Li-ion batteries, *Chem. Eng. J.* 328 (2017) 591–598.
- [18] X.L. Sheng, T. Li, M. Sun, G.J. Liu, Q.Y. Zhang, Z.B. Ling, S.W. Gao, F.Y. Diao, J. Z. Zhang, F. Rosei, Y.Q. Wang, Flexible electrospun iron compounds/carbon fibers: phase transformation and electrochemical properties, *Electrochim. Acta* 407 (2022), 139892.
- [19] M.E. Im, P.C. De, J.Y. Kim, H.S. Choi, J.H. Kim, J.P. Kim, J. Kim, S.Y. Jeong, C. R. Cho, Enhanced electrochemical performance of template-free carbon-coated iron(II, III) oxide hollow nanofibers as anode material for lithium-ion batteries, *J. Power Sources* 284 (2015) 392–399.
- [20] W. Xu, L. Liu, W. Weng, High-performance supercapacitor based on MnO/carbon nanofiber composite in extended potential windows, *Electrochim. Acta* 370 (2021), 137713.
- [21] Q. Xie, Y. Zhang, D. Xie, P. Zhao, Nitrogen-enriched graphitic carbon encapsulated Fe₃O₄/Fe₃C/Fe composite derived from EDTA-Fe(III) sodium complex as LiBs anodes with boosted performance, *J. Electroanal. Chem.* 857 (2020), 113749.
- [22] Z. Zhou, C. Lai, L. Zhang, Y. Qian, H. Hou, D.H. Reneker, H. Fong, Development of carbon nanofibers from aligned electrospun polyacrylonitrile nanofiber bundles and characterization of their microstructural, electrical, and mechanical properties, *Polymer* 50 (2009) 2999–3006.
- [23] T. Li, S.W. Gao, K. Li, G.J. Liu, X.L. Sheng, D.W. Shang, L.M. Wu, S.J. Chen, Y. Q. Wang, S.H. Wu, Tailoring the phase evolution of molybdenum-based nanocrystals in carbon nanofibers for enhanced performance of lithium-ion batteries, *J. Alloy. Compd.* 934 (2023), 168042.
- [24] T. Yamashita, P. Hayes, Analysis of XPS spectra of Fe²⁺ and Fe³⁺ ions in oxide materials, *Appl. Surf. Sci.* 254 (2008) 2441–2449.
- [25] J.P. Hong, S.B. Lee, Y.W. Jung, J.H. Lee, K.S. Yoon, K.W. Kim, C.O. Kim, C.H. Lee, M.H. Jung, Room temperature formation of half-metallic Fe₃O₄ thin films for the application of spintronic devices, *Appl. Phys. Lett.* 83 (2003) 1590–1592.
- [26] M.E. Im, D. Pham-Cong, J.Y. Kim, H.S. Choi, J.H. Kim, J.P. Kim, J. Kim, S.Y. Jeong, C.R. Cho, Enhanced electrochemical performance of template-free carbon-coated iron(II, III) oxide hollow nanofibers as anode material for lithium-ion batteries, *J. Power Sources* 284 (2015) 392–399.
- [27] J.J. Wang, X.Y. Xue, Y.Q. Wang, Tuning the structural and magnetic properties of electrospun strontium-iron-oxide nanofibers with different stoichiometry, *Mater. Charact.* 200 (2023), 112884.
- [28] B.H. Xu, L.B. Yu, X. Zhao, H.R. Wang, C. Wang, L.Y. Zhang, G.L. Wu, Simple and effective synthesis of zinc ferrite nanoparticle immobilized by reduced graphene oxide as anode for lithium-ion batteries, *J. Colloid Interface Sci.* 584 (2021) 827–837.
- [29] D. Wilson, M.A. Langell, XPS analysis of oleylamine/oleic acid capped Fe₃O₄ nanoparticles as a function of temperature, *Appl. Surf. Sci.* 303 (2014) 6–13.
- [30] Y.W. Liu, S.W. Sun, J. Han, C. Gao, L. Fan, R. Guo, Multi-yolk-shell MnO@carbon nanopomegranates with internal buffer space as a lithium ion battery anode, *Langmuir* 37 (2021) 2195–2204.
- [31] L. Li, A. Kovalchuk, H. Fei, Z. Peng, Y. Li, N.D. Kim, C. Xiang, Y. Yang, G. Ruan, J. M. Tour, Enhanced cycling stability of lithium-ion batteries using graphene-wrapped Fe₃O₄-graphene nanoribbons as anode materials, *Adv. Energy Mater.* 5 (2015), 1500171.
- [32] D.W. Jung, J.H. Jeong, S.W. Han, E.S. Oh, Electrochemical performance of potassium-doped wustite nanoparticles supported on graphene as an anode material for lithium ion batteries, *J. Power Sources* 315 (2016) 16–28.
- [33] Y. Xiao, X. Wang, W. Wang, D. Zhao, M.H. Cao, Engineering hybrid between MnO and N-doped carbon to achieve exceptionally high capacity for lithium-ion battery anode, *ACS Appl. Mater. Interfaces* 6 (2014) 2051–2058.
- [34] D. Chen, C. Feng, Y. Han, B. Yu, W. Chen, Z. Zhou, N. Chen, J.B. Goodenough, W. He, Origin of extra capacity in the solid electrolyte interphase near high-capacity iron carbide anodes for Li ion batteries, *Energy Environ. Sci.* 13 (2020) 2924–2937.
- [35] J. Li, W. Wen, G. Xu, M. Zou, Z. Huang, L. Guan, Fe-added Fe₃C carbon nanofibers as anode for Li ion batteries with excellent low-temperature performance, *Electrochim. Acta* 153 (2015) 300–305.
- [36] M.V. Reddy, G.V. Subba Rao, B.V.R. Chowdari, Metal oxides and oxysalts as anode materials for Li ion batteries, *Chem. Rev.* 113 (2013) 5364–5457.
- [37] H.L. Lyu, J.R. Liu, S. Qiu, Y.H. Cao, C.X. Hu, S.M. Guo, Z.H. Guo, Carbon composite spun fibers with *in situ* formed multicomponent nanoparticles for a lithium-ion battery anode with enhanced performance, *J. Mater. Chem. A* 4 (2016) 9881–9889.
- [38] Y. Shi, B. Guo, S.A. Corr, Q. Shi, Y. Hu, K.R. Heier, L. Chen, R. Seshadri, G. D. Stucky, Ordered mesoporous metallic MoO₂ materials with highly reversible lithium storage capacity, *Nano Lett.* 9 (2009) 4215–4220.
- [39] Q. Tang, Z. Shan, L. Wang, X. Qin, MoO₂-graphene nanocomposite as anode material for lithium-ion batteries, *Electrochim. Acta* 79 (2012) 148–153.
- [40] Y. Sun, X. Hu, J. Yu, Q. Li, W. Luo, L. Yuan, W. Zhang, Y. Huang, Morphosynthesis of a hierarchical MoO₂ nanoarchitecture as a binder-free anode for lithium-ion batteries, *Energy Environ. Sci.* 4 (2011) 2870–2877.
- [41] Y.G. Huang, X.L. Lin, X.H. Zhang, Q.C. Pan, Z.X. Yan, H.Q. Wang, J.J. Chen, Q. Y. Li, Fe₃C@carbon nanocapsules/expanded graphite as anode materials for lithium ion batteries, *Electrochim. Acta* 178 (2015) 468–475.
- [42] L.W. Su, Z. Zhou, P.W. Shen, Core-shell Fe@Fe₃C/C nanocomposites as anode materials for Li ion batteries, *Electrochim. Acta* 87 (2013) 180–185.
- [43] L. Guo, H. Sun, C. Qin, W. Li, F. Wang, W. Song, J. Du, F. Zhong, Y. Ding, Flexible Fe₃O₄ nanoparticles/N-doped carbon nanofibers hybrid film as binder-free anode materials for lithium-ion batteries, *Appl. Surf. Sci.* 459 (2018) 263–270.
- [44] M. Sun, S. Li, J. Zou, Z. Cui, Q. Zhang, F. Schiettekatte, D. Barba, B. Liu, Y. Wang, Graphene-wrapped ZnMn₂O₄ nanoparticles with enhanced performance as lithium-ion battery anode materials, *Nano* 15 (2020), 2050117.
- [45] J. Zou, B. Liu, H. Liu, Y. Ding, T. Xin, Y. Wang, Facile synthesis of interconnected mesoporous ZnMn₂O₄ nano-peanuts for Li-storage *via* distinct structure design, *Mater. Res. Bull.* 107 (2018) 468–476.
- [46] M. Sun, X. Sheng, S. Li, Z. Cui, T. Li, Q. Zhang, F. Xie, Y. Wang, Construction of porous CoTiO₃ microrods with enhanced performance as lithium-ion battery anode, *J. Alloy. Compd.* 926 (2022), 166809.
- [47] Q. Wu, R. Xu, R. Zhao, X. Zhang, W. Li, G. Diao, M. Chen, Tube-in-tube composite nanofibers with high electrochemistry performance in energy storage applications, *Energy Storage Mater.* 19 (2019) 69–79.